Received 1 October; accepted 30 December 1997.

1. Friedel, J. *Dislocations* (Pergamon, Oxford, 1964).
2. Abraham, F. F. *et al.* Instability dynamics in three-dimensional fracture: an atomistic approach. *J. Mech. Phys. Solids* **45,** 1461–1471 (1997).
3. Devincre, B. & Kubin, L. P. Mesoscopic simulations of dislocations and plasticity *Mater. Sci. Eng.* **A234–236,** 8–14 (1997).
4. Devincre, B. & Kubin, L. Simulations of forest interactions and strain hardening in FCC crystals. *Modelling Simul. Mater. Sci. Eng.* **2,** 559–570 (1994).
5. Abraham, F. F. On the transition from brittle to plastic failure in breaking a nanocrystal under tension. *Europhys. Lett.* **38,** 103–106 (1997).
6. Hirth, J. P. & Lothe, J. *Theory of Dislocations* 2nd edn 792–806 (Wiley, New York, 1982).
7. Nabarro, F. R. N. *Theory of Crystal Dislocations* (Oxford Univ. Press, London, 1967).
8. Prinz, F. & Argon, A. S. Dislocation cell formation during plastic deformation of copper single crystals. *Phys. Status Solidi A* **57,** 741–753 (1980).
9. Korner, A. & Karnthaler, H. P. Weak-beam studies of composite dislocations gliding on (001) planes in Si. *Phil. Mag.* **44,** 275–284 (1981).

Acknowledgements. This work originated at a collaborative workshop on materials modelling held at the Institute for Theoretical Physics, UCSB, during March 1997. F.F.A. acknowledges the use of the Cornell Theory Center, which receives funding from the NSF and New York State; B.D. and L.K. acknowledge the support of CNRS through the GdR programme on mesoscopic simulations and modelling in metallurgy; V.B. and S.Y. acknowledge support from LLNL; and V.B. acknowledges support from the Alcoa Foundation.

Correspondence and requests for materials should be addressed to V.B. (e-mail: vasily@mit.edu).

Impact energy measurement in time-of-flight mass spectrometry with cryogenic microcalorimeters

G. C. Hilton*, John M. Martinis*, D. A. Wollman*, K. D. Irwin*, L. L. Dulcie*, Daniel Gerber†, Patrick M. Gillevet‡ & Damian Twerenbold†

** National Institute of Standards and Technology, Boulder, Colorado 80303, USA*
† Institut de Physique de l'Université Rue A.-L. Breguet 1, CH-2000 Neuchâtel, Switzerland, and GenSpec SA, case postale 120, CH-2017 Boudry, Switzerland
‡ Institute of Bioscience, Bioinformatics, and Biotechnology, George Mason University, Manassas, Virginia 22210, USA

Time-of-flight mass spectrometry—most notably matrix-assisted laser-desorption-ionization time-of-flight (MALDI-TOF) spectrometry[1]—is an important class of techniques for the study of proteins and other biomolecules[2]. Although these techniques provide excellent performance for masses up to about 20,000 daltons, there has been limited success in achieving good mass resolution at higher masses. This is because the sensitivity of the microchannel plate (MCP) detectors used in most systems decreases rapidly with increasing particle mass, limiting the utility of MCP detectors for very large masses. It has recently been proposed that cryogenic particle detectors may provide a solution to these difficulties[3]. Cryogenic detectors measure the thermal energy deposited by the particle impact, and thus have a sensitivity that is largely independent of particle mass. Recent experiments[4–6] have demonstrated the sensitivity of cryogenic particle detectors to single biomolecules, a quantum efficiency several orders of magnitude larger than the MCP detectors, and sensitivity to masses as large as 750,000 daltons. Here we present results demonstrating an order of magnitude better energy resolution than previous measurements, allowing direct determination of particle charge state during acceleration[7]. Although application of these detectors to practical mass spectrometry will require further development of the detectors and cryogenics, these detectors can be used to elucidate the performance-limiting processes that occur in such systems.

In the past several years, significant progress has been made in developing high-performance cryogenic detectors for applications such as infrared bolometry and X-ray, visible and ultraviolet spectroscopy. These detectors fall into two classes: non-equilibrium devices such as superconducting tunnel junctions (STJs)[8,9], and equilibrium devices such as microcalorimeters[10–13]. The previous experiments[4,5] with cryogenic particle detectors for mass spectrometry used STJs, which fail to record the total impact energy because they are insensitive to the fraction of impact energy deposited as phonons with energy less than the superconducting gap. In this experiment we used a normal-insulator-superconductor microcalorimeter fabricated on a thin Si_3N_4 membrane, which detects all of the thermal energy deposited by a particle impact. Although the speed and energy resolution performance of our detector is sufficient for this preliminary experiment, experience with other applications indicate that significantly better performance should be possible in the future. It is important to note that the collection area of the cryogenic detectors studied is more than 10^4 times smaller than typical MCP detectors. Although this size can be improved in the future, the overall sensitivity (the product of quantum efficiency and collection area) of this detector is significantly less than MCP detectors except at extremely large (>100,000 daltons) masses[6].

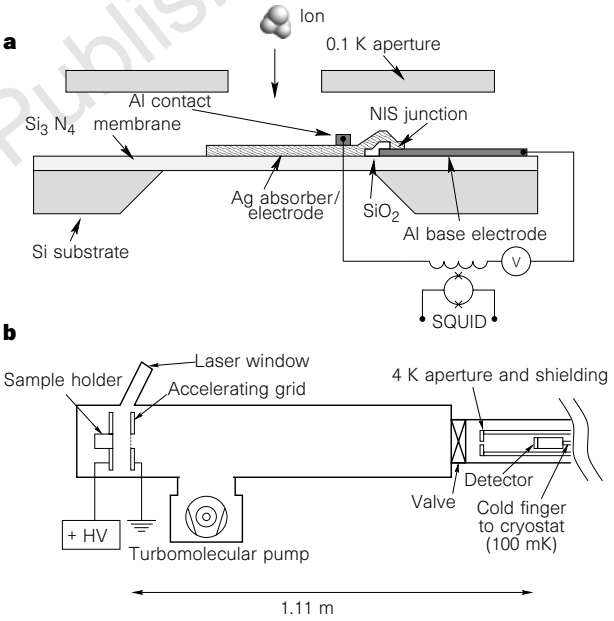

Figure 1 Details of experimental apparatus. **a**, Cross-section of the normal-insulator-superconductor (NIS) microcalorimeter. An accelerated molecule flies through a 200-μm-diameter 0.1 K aperture and strikes the absorber (a 100-nm-thick Ag film measuring 200 μm × 200 μm deposited on a 0.5-μm-thick Si_3N_4 membrane), raising the absorber temperature. This temperature rise is detected as a current pulse produced by a voltage-biased NIS junction, which consists of a thinly oxidized Al electrode in contact with the absorber. The junction current is measured by a SQUID preamplifier. Contacts to the detector are provided by superconducting Al leads which carry electrical current but do not conduct heat. **b**, Schematic view of our MALDI-TOF spectrometer indicating detector placement and infrared shielding. The infrared shielding consists of a 1-mm-diameter aperture cooled to 4 K and placed 10 cm away from the detector. Ions are created when laser light pulses (337 nm, 3 ns, maximum power 100 μJ) strike the probe plate. Ions are accelerated by an electric field between the probe plate and the grounded fine-mesh accelerating grid. Vacuum in the spectrometer is provided by a 110 l s^{-1} turbomolecular pump, attaining a base pressure in the 100-mm-diameter flight tube of 2×10^{-5} Pa (1.5×10^{-7} torr). Two proteins were studied, lysozyme (mass 14,300 daltons) and bovine serum albumin (BSA, mass 66,430 daltons). In both cases proteins solutions were prepared by combining 1 mg of protein with 1 ml of a 0.1% trifluoroacetic acid H_2O solution. The matrix solution consisted of 100 mg sinapinic acid (mass 224 daltons) dissolved in 6 ml of ethanol and 4 ml H_2O. Probes were prepared by mixing 40 μl each of the probe and matrix solutions and allowing the mixture to dry in air on the probe plate.

Our detector, similar to that described elsewhere[12], is shown in cross-section in Fig. 1a, along with the external circuit used to bias and read out the detector. The detector current is measured using a high-speed low-noise series-array superconducting quantum interference device (SQUID) amplifier[14]. The detector is cooled to its operating temperature of 100 mK using a liquid-helium cryostat with an adiabatic demagnetization refrigerator. The cryostat is coupled to a MALDI-TOF spectrometer as shown in Fig. 1b.

The detector energy scale was calibrated using X-rays from a ^{55}Fe radioactive source mounted in the detector line of sight. The energy resolution of the detector was measured for X-rays using several thousand digitized waveforms. The energy of each event was determined using Weiner optimal filtering, and the resolution was determined by fitting the resulting energy histogram to a normal distribution. For X-rays we obtained an energy resolution of 92 eV full-width at half-maximum (FWHM). In Fig. 2a we show a digitized detector waveform obtained from one laser strike on a protein target of bovine serum albumin (BSA, mass 66,430 daltons).

In Fig. 2b we show a scatter plot of impact energies versus arrival times for a sample of BSA in a sinapinic acid matrix (mass 224 daltons) for an accelerating voltage, U, of 20 kV. The plot shows a clear energy banding, caused by the discrete ionization states of the particles. The utility of impact energy resolution is clearly shown by examining two groupings of points, one at $t_1 = 146\,\mu s$ and $E_1 = 10$ keV, and the other at $t_2 = 103\,\mu s$ and $E_2 = 20$ keV. Calculating the mass corresponding to t_1 using $m = (2zUt^2)/l^2$ where l is the length of the flight tube and taking charge $z = e$, we find that $m_1 = 66{,}600$ daltons. If we similarly calculate the mass corresponding to t_2 with $z = 2e$, we find $m_2 = 66{,}400$ daltons. Thus we associate the first grouping with BSA^+ and the second grouping with BSA^{2+}. Additional groupings in Fig. 2b include sinapinic acid ($m = 224$, $t = 10\,\mu s$) and an unidentified fragment with $m \approx 14{,}000$ daltons ($t = 67\,\mu s$). There is also a small grouping at the same time-of-flight as the BSA^+ group with twice the energy of the BSA^+ group. This group is due to either doubly charged BSA dimers or the simultaneous arrival of two singly charged BSA monomers.

A surprising feature of Fig. 2b is that the thermal energy E_d deposited in the microcalorimeter by a particle impact is roughly half of the particle's kinetic energy zU. This difference implies that a significant fraction of the particle's kinetic energy is not converted to thermal energy in the detector. Thus impact cannot be modelled as a rigid molecule striking, and sticking to, the detector. Processes that might account for the missing energy include fragmentation of the molecule hitting the detector and ejection of molecular fragments.

To investigate further the dependence of impact energy on molecule type, we show in Fig. 3 the ratio of deposited to kinetic energy versus kinetic energy for three different molecules. At low

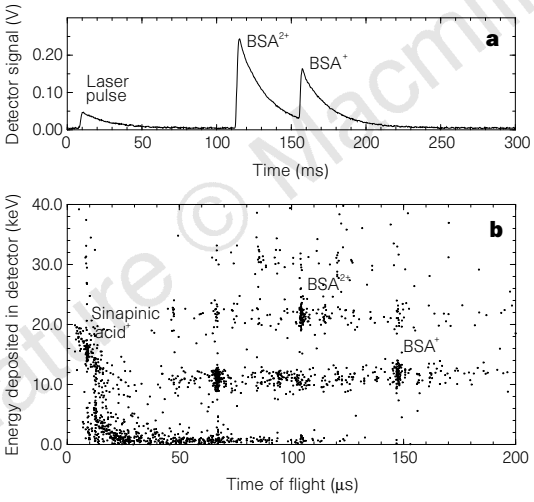

Figure 2 Experimental data obtained for the protein BSA. **a**, An example time trace for one laser event with three detector pulses. The first pulse is due to reflected laser light striking the detector, the remaining pulses are due to ions and are identified as BSA^{2+} and BSA^+. **b**, A scatter plot of detector energy versus ion time of flight for BSA with an acceleration voltage of 20 kV. Clear energy banding is shown for ions of different charge. The ratio of energy deposited in the detector to ion kinetic energy (E_d/zU) is 0.59 for BSA^+ and 0.74 for singly charged sinapinic acid. This scatter plot was generated by extracting time and energy information from time traces for several thousand laser events. For each laser pulse we acquired a time trace consisting of 4,096 samples of the SQUID preamplifier output at either 50-ns or 100-ns intervals using a 20 MHz 12-bit analog-to-digital converter. Particle impact times were determined by an edge detection algorithm applied to the time traces and particle impact energies were extracted by comparing the impact waveforms with a calibrated waveform derived from X-ray events. The signal rise time (1.2 μs) allowed us to determine the time of impact within ~200 ns. Potential difficulties of pulse pile-up due to the slow detector fall time (17 μs) are mitigated by the detector linearity, the 12 bit digitization, and the small number of particle strikes per launch event.

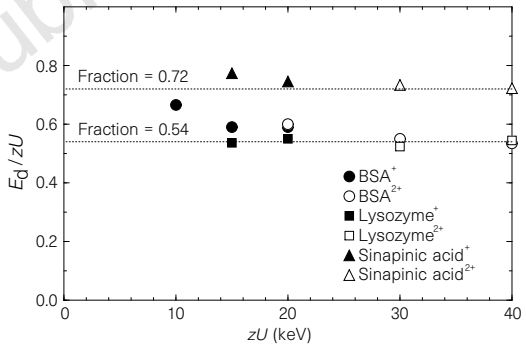

Figure 3 Plot of the ratio of impact energy to kinetic energy versus kinetic energy for each ion type. The ratio is determined by dividing the centroid of the impact energy distribution for an identified particle grouping by the kinetic energy of that grouping. For the heavier ions (lysozyme, BSA) this fraction approaches 0.54 for large acceleration potentials, whereas for the lighter ion (sinapinic acid) the asymptote is 0.72.

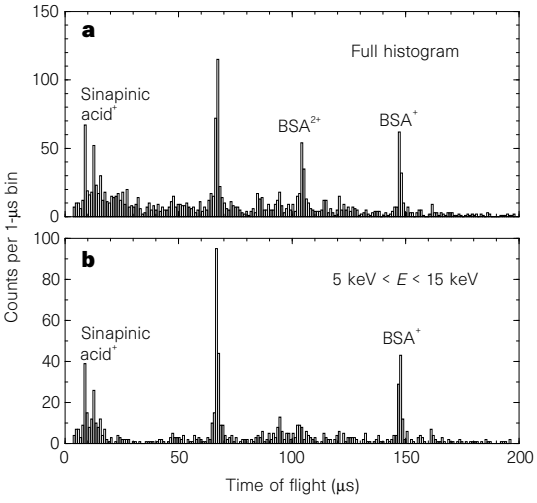

Figure 4 Time-of-flight spectrum for BSA with an acceleration voltage of 20 kV. **a**, Full histogram with all acquired points. **b**, Histogram containing only those points whose deposited energy is between 5 and 15 kV. The peak due to doubly ionized BSA, as well as much of the background, is removed by this selection.

kinetic energies, we see indications of an increase in fractional energy deposition, as might be expected as there is less energy available to deform the ion. Presumably E_d/zU approaches 1 at very low kinetic energies. At large kinetic energies, the proteins deposit about half of their kinetic energy in the detector, while the much lighter sinapinic acid deposits nearly three-quarters of its kinetic energy. Because there are many more bonds in the larger molecules, it is not surprising that more of the kinetic energy is lost in impact ejection or fragmentation. Although we do not fully understand the origin of the asymptotic 50% impact energy observed at high kinetic energies for lysozyme and BSA, preliminary experiments with immunoglobulin G (IgG, 155,000 daltons) show that this same asymptotic limit holds for larger masses. Because the total bond energy of sinapic acid is less than the impact energy deficit, we believe that this is evidence that ejection is the dominant energy loss mechanism. In the only previous measurement of fractional energy deposition using STJs[5], the measured impact energy was ~20% of the kinetic energy. The lower value of E_d/zU obtained with the STJ detectors is not surprising, given the phonon loss mechanisms previously discussed.

Histograms of arrival times for BSA are plotted in Fig. 4a using all particle impacts, and in Fig. 4b using only those events with impact energies between 5 and 15 keV. In the selective plot of Fig. 4b, both the background and the BSA^{2+} peak have been greatly reduced. Similar histograms were used to determine the mass and energy resolution of the mass spectrometer. For the BSA monomer peak, we obtain a timing resolution of 1.3 μs (FWHM), implying a mass resolution $M/\Delta M$ of 56, similar to results obtained elsewhere[15]. An energy resolution of 1.7 keV (FWHM) was obtained, which is significantly worse than both the 92 eV (FWHM) resolution obtained with X-rays and the kinetic energy uncertainty implied by the time-of-flight uncertainty, inferring that the energy lost to ejection and fragmentation during impact must be variable.

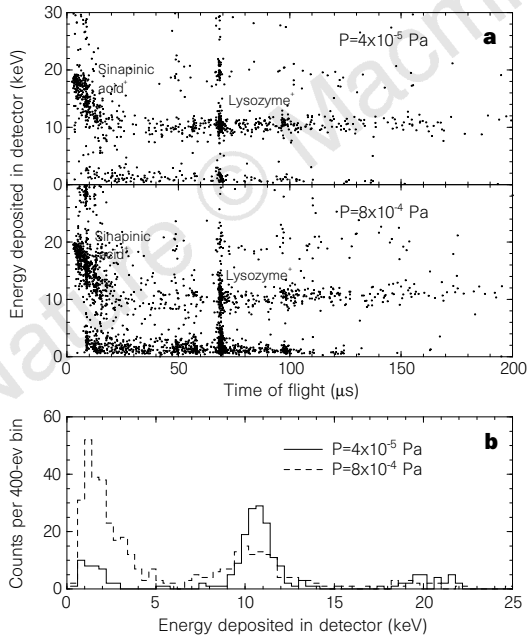

Figure 5 Experimental data showing additional scattering and changes in impact energy resolution due to gas phase scattering. **a**, Scatter plots for lysozyme (mass 14,300 daltons) taken at two different pressures. At the higher pressure, many more ions with low impact energy are observed. This effect is due to gas-phase scattering and fragmentation in the flight tube. The mean free path for lysozyme collision with ambient gas molecules is 1/3 of the flight tube length in the high-pressure case and 6 times the flight tube length in the low-pressure case. **b**, Histogram of impact energies for the expected arrival time of lysozyme$^+$ (68 μs $< t <$ 70 μs). The data at higher pressure show both a low-energy peak and an enhanced low-energy tail of the 11-keV peak. These features are due to small and large fragments of the lysozyme caused by gas-phase fragmentation in the free-flight region.

Measurement of impact energy with the microcalorimeter allows us to explore the effect of background gas pressure in the spectrometer. As background pressure increases, gas-phase collisions in both the acceleration and free-flight regions increase, decreasing the quality of the spectra. The effect of pressure is clearly shown in Fig. 5a, which shows scatter-plot spectra for lysozyme (mass 14,300 daltons) taken at 4×10^{-5} Pa (3×10^{-7} torr) and 8×10^{-4} Pa (6×10^{-6} torr). At high pressure, we observe a significant increase in the number of low-energy (<5 keV) particles arriving at the predicted time of flight for lysozyme. We attribute this effect to fragmentation of the lysozyme ions owing to collisions with background gas in the free-flight region of the spectrometer. Fragments produced during free flight carry less kinetic energy, but travel at velocities nearly equal to that of the original molecule and arrive at the expected time for lysozyme. On the other hand, fragmentation during acceleration would affect the velocity and cannot explain these events. In Fig. 5b we show the effect on this fragmentation on impact energy. Here we plot a histogram of impact energies for those particles arriving with near the predicted time of flight for lysozyme. The histograms show that at low pressure there are many more low-energy events which are caused by small fragments, and a broadening of the primary 11-keV peak by a low-energy tail which is caused by larger fragments.

Insight into the effect of gas phase collisions can be gained by estimating the cross-sections and mean free paths of the proteins. From X-ray structure data for lysozyme[16], we estimate the molecular cross-section for gas-phase scattering to be 15 nm^2. With this cross-section, the mean free path for lysozyme at a nitrogen gas pressure of 4×10^{-5} Pa is ~6 m, whereas at 8×10^{-4} Pa the mean free path is 0.3 m. Thus at the higher pressure considered in Fig. 5, lysozyme will typically undergo 3–4 collisions in traversing the flight tube. Assuming hard-sphere elastic collisions between a 20-keV lysozyme ion and an ambient-temperature nitrogen molecule, the maximum energy transferred per collision is 160 eV. This energy is more than sufficient to break bonds in lysozyme, supporting our conclusion that fragmentation occurs during flight. These results are similar to those reported elsewhere[17], where fragmentation caused in the free-flight region was measured by subsequent deceleration of ions, allowing measurement of the relative concentration of neutral fragments relative to unfragmentated ions to yield the fragmentation cross-section. For a protein similar to lysozyme (cytochrome *c*), a cross-section of 14.1 nm^2 was measured, consistent with our results.

A similar calculation of the cross-section for BSA shows that gas-phase collisions cannot explain the mass resolution obtained with our spectrometer. Using X-ray data[18] we estimate the cross-section of BSA to be 30 nm^2, giving a mean free path of 3 m at the normal operating pressure. Assuming that the maximum energy transferred per gas collision is 80 eV, and that each molecule undergoes on average less than one collision, the worst case estimate for mass resolution $M/\Delta M$ is 250, which is better than the observed value of 56. In the present experiments, where mass resolution is not limited by gas collisions or detector response time, we conclude that the greatest contributions to mass uncertainty arise during launch and acceleration. □

Received 17 April; accepted 16 December 1997.

1. Karas, M. & Hillenkamp, F. Laser desorption ionization of proteins and molecular masses exceeding 10000 Daltons. *Anal. Chem.* **188,** 2299–2301 (1988).
2. Siuzdak, G. The emergence of mass spectrometry in biochemical research. *Proc. Natl. Acad. Sci. USA* **91,** 11290–11297 (1994).
3. Twerenbold, D. Biopolymer mass spectrometer with cryogenic particle detectors. *Nucl. Instrum. Meth. Phys. Res. A* **370,** 253–255 (1996): US Patent No. 5,640,010 (1997).
4. Twerenbold, D. *et al.* Detection of single macromolecules using a cryogenic particle detector coupled to a biopolymer mass spectrometer. *Appl. Phys. Lett.* **68,** 3503–3505 (1996).
5. Frank, M., Mears, C. A., Labov, S. E. & Benner, W. H. High-efficiency detection of 66 000 Da protein

molecules using a cryogenic detector in a matrix-assisted laser desorption/ionization time-of-flight mass spectrometer. *Rapid Commun. Mass Spectrom.* **10,** 1946 (1996).
6. Labov, S. E. *et al.* Cryogenic detector development at LLNL: ultraviolet, X-ray, gamma-ray and biomolecule spectroscopy. in *Proc. 7th Int. Workshop on Low Temperature Detectors* (ed. Cooper, S.) 82–95 (Max Planck Institute of Physics, Munich, 1997).
7. Benner, W. H. *et al*. Simultaneous measurement of flight time and energy of large matrix-assisted laser desorption ions with a superconducting tunnel junction detector. *J. Am. Soc. Mass Spectrom.* **8,** 1094–1102 (1997).
8. Mears, C. A. *et al.* Analysis of pulse shape from a high resolution superconducting tunnel junction X-ray spectrometer. *Nucl. Instrum. Meth. Phys. Res. A* **370,** 53–56 (1996).
9. Peacock, A. *et al*. Single optical photon detection with a superconducting tunnel junction. *Nature* **381,** 135–137 (1996).
10. McCammon, D., Cui, W., Juda, M., Morgenthaler, J. & Zhang, J. Thermal calorimeters for high resolution X-ray spectroscopy. *Nucl. Instrum. Meth. Phys. Res. A* **326,** 157–165 (1993).
11. Irwin, K. D., Hilton, G. C., Wollman, D. A. & Martinis, J. M. X-ray detection using a superconducting transition-edge sensor microcalorimeter with electrothermal feedback. *Appl. Phys. Lett.* **69,** 1945–1947 (1996).
12. Nahum, M. & Martinis, J. M. Hot-electron microcalorimeters as high-resolution x-ray detectors. *Appl. Phys. Lett.* **66,** 3203–3205 (1995).
13. Martinis, J. M. Hot-electron-microcalorimeters with 0.25 mm^2 area. *Nucl. Instrum. Meth. Phys. Res. A* **370,** 171–172 (1996).
14. Welty, R. P. & Martinis, J. M. A series array of DC SQUIDs. *IEEE Trans. Mag.* **27,** 2924–2926 (1991).
15. Schreiner, M., Strupat, K., Lottspeich, F. & Eckershorn, C. Ultraviolet matrix assisted laser desorption ionization-mass spectrometry of electroblotted proteins. *Electrophoresis* **17,** 954–961 (1996).
16. Vaney, M. C., Maignan, S., Ries-Kautt, M. & Ducruix, A. *Protein Data Bank File No. 1931* (Brookhaven National Laboratory Protein Data Bank, 1995).
17. Spengler, B., Kirsch, D. & Kaufmann, R. Fundamental aspects of postsource decay in matrix-assisted laser desorption mass spectrometry. 1. Residual gas effects. *J. Phys. Chem.* **96,** 9678–9684 (1992).
18. He, X. M. & Carter, D. C. Atomic structure and chemistry of human serum albumin. *Nature* **358,** 209–215 (1992).

Correspondence and requests for materials should be addressed to G.H. (e-mail hilton@boulder.nist.gov).

Increased stratospheric ozone depletion due to mountain-induced atmospheric waves

K. S. Carslaw*, M. Wirth†, A. Tsias*, B. P. Luo*, A. Dörnbrack†, M. Leutbecher†, H. Volkert†, W. Renger†, J. T. Bacmeister‡, E. Reimer§ & Th. Peter*

* *Max-Planck-Institut für Chemie, Postfach 3060, Mainz 55020, Germany*
† *DLR, Oberpfaffenhofen, 32230 Wessling, Germany*
‡ *Code 7641, Naval Research Laboratory, Washington DC, 20375, USA*
§ *Institut für Meteorologie, Carl-Heinrich-Becker Weg, 12165, Berlin 41, Germany*

Chemical reactions on polar stratospheric cloud (PSC) particles are responsible for the production of reactive chlorine species (chlorine 'activation') which cause ozone destruction[1]. Gas-phase deactivation of these chlorine species can take several weeks in the Arctic winter stratosphere, so that ozone destruction can be sustained even in air parcels that encounter PSCs only intermittently[2,3]. Chlorine activation during a PSC encounter proceeds much faster at low temperatures when cloud particle surface area and heterogeneous reaction rates are higher[4]. Although mountain-induced atmospheric gravity waves are known to cause local reductions in stratospheric temperature of as much as 10–15 K (refs 5–9), and are often associated with mesoscale PSCs[10–12], their effect on chlorine activation and ozone depletion has not been considered. Here we describe aircraft observations of mountain-wave-induced mesoscale PSCs in which temperatures were 12 K lower than expected synoptically. Model calculations show that despite their localized nature, these PSCs can cause almost complete conversion of inactive chlorine species to ozone-destroying forms in air flowing through the clouds. Using a global mountain-wave model[8], we identify regions where mountain waves can develop, and show that they can cause frequent chlorine activation of air in the Arctic stratosphere. Such mesoscale processes offer a possible explanation for the under-prediction of reactive chlorine concentrations and ozone depletion rates calculated by three-dimensional models of the Arctic stratosphere[13–17].

A stratospheric mountain-wave-induced PSC observed by airborne lidar over Scandinavia is shown in Fig. 1a. An ice cloud ('mother-of-pearl cloud') is apparent in the lidar signal as the yellow and red streaks of high aerosol backscatter ratio at around 22 km altitude. The presence of this cloud indicates strong localized cooling due to mountain-wave activity because the ice frost point at this altitude ($T_{frost} \approx 185.7$ K for 5 parts per million by volume, p.p.m.v., water vapour) is considerably lower than the temperature of 193 K derived from synoptic analyses from the European Centre for Medium-Range Weather Forecasts (ECMWF). The ice cloud is surrounded by a liquid PSC, which is visible in the lidar signal as a distinct wave-disturbed aerosol layer between 21 and 24 km altitude[12]. This probably formed because of absorption of HNO_3 and H_2O by the background liquid H_2SO_4/H_2O aerosols[18]. On the day of measurement, the research aircraft made several flights across and parallel to the mountains[12]. All the measurements are consistent with a mountain-induced PSC extending over several hundred kilometres, with dense ice clouds over the highest orography. Analysis of other nearby clouds and of the general mesoscale situation[12] indicates that the cloud in Fig. 1, including the liquid PSC, was probably embedded in a broader mesoscale minimum temperature.

Here we use data from this short flight segment to demonstrate the potential effect of even such small mesoscale PSCs on stratospheric chemistry. Two features of this flight make it ideal for studying the effect of such clouds on the chemistry of air parcels flowing over the mountains. First, the observation was made by flying directly upwind, which we term quasi-lagrangian. Second, the wave-cloud can be considered as quasi-stationary during the short time required for air parcels to traverse the wave, which is ~30 minutes. This was confirmed by repeated measurements of other mountain-wave clouds on the same day which revealed quasi-stationarity on a timescale of ~4 hours. Also, simulations using the mesoscale model MM5[12] indicate that gravity waves in this region were persistent for at least 1 hour. Together, the quasi-lagrangian observation and the stationarity of the cloud allow the particle streaks to be considered as air-parcel trajectories. One such trajectory is indicated by the white line in Fig. 1a, with a temperature shown in Fig. 1c. Thus, the trajectory that we use to study air-parcel microphysics and chemistry was constructed from aerosol layers apparent in the lidar signal, rather than from predictions of the MM5 mesoscale model. Although the MM5 model reproduces very well the general pattern of cooling over the mountains on the day of measurement[12], resolution limitations mean that the small-scale structure and deep temperature minima apparent in Fig. 1a cannot easily be resolved.

The air-parcel temperature is critical for the microphysical and chemical modelling of the cloud. The existence of ice clearly indicates a departure from synoptic conditions, but the minimum temperature attained in the wave is even lower than the frost point. This minimum temperature can be calculated as follows: at the point of maximum backscatter (point 1 in Fig. 1a) the ice particles are transiently in equilibrium with the gas phase, which implies that the temperature must be below the frost point ($T < T_{frost}$). How much point 1 is below the frost point depends on the amount of water vapour condensed as ice. From our microphysical model simulation, we calculate the actual temperature at point 1 to be 183.8 ± 0.5 K. Temperatures at other locations in the wave can then be calculated from this reference temperature by assuming dry adiabatic behaviour. The minimum temperature in the wave occurs ~280 m higher in altitude (point 2 in Fig. 1a) and is therefore ~181 K, some 12 K lower than synoptic. The rather constant offset of 8–10 K between the synoptic temperature and the temperature in the wave reflects the fact that the PSC is embedded in a larger mesoscale minimum, and does not indicate a significant warm bias